





In-medium nucleon-nucleon cross sections from characteristics of nuclear giant resonances and nuclear stopping power

Yi-Dan Song (宋一丹) ^{1,2} Rui Wang (王睿) ^{2,3,*} Zhen Zhang (张振) ^{4,†} and Yu-Gang Ma (马余刚) ^{2,5,‡}

¹Department of Physics, College of Science, University of Shanghai for Science and Technology, Shanghai 200093, China

²Key Laboratory of Nuclear Physics and Ion-beam Application (MOE), and Institute of Modern Physics, Fudan University, Shanghai 200433, China

³Shanghai Institute of Applied Physics, Chinese Academy of Sciences, Shanghai 201800, China

⁴Sino-French Institute of Nuclear Engineering and Technology, Sun Yat-sen University, Zhuhai 519082, China

⁵Shanghai Research Center for Theoretical Nuclear Physics, NSFC and Fudan University, Shanghai 200438, China



(Received 30 July 2023; revised 22 October 2023; accepted 8 November 2023; published 6 December 2023)

Based on the Boltzmann-Uehling-Uhlenbeck (BUU) transport equation, a medium correction to the elastic nucleon-nucleon (NN) cross sections is given by comparing the width of the isovector giant dipole resonance in ^{208}Pb and the nuclear stopping obtained from the BUU equation with those from experimental measurements. For the nuclear stopping, we choose the scaled rapidity distributions and the nuclear stopping power $vartl$, denoted as the ratio of the variances of the transverse to that of the longitudinal rapidity distributions, of central $^{197}\text{Au} + ^{197}\text{Au}$ collisions at the energy of 150A MeV measured by the INDRA and the FOPI collaborations. This enables us to provide a unified medium correction of elastic NN cross sections for distinct energy regimes. A reliable in-medium NN cross section, as given here, will reduce the uncertainties of the BUU equation when applying it to nuclear collective motion and heavy-ion collisions to extract the information of the nuclear equation of state.

DOI: [10.1103/PhysRevC.108.064603](https://doi.org/10.1103/PhysRevC.108.064603)

I. INTRODUCTION

The transport model of heavy-ion collisions (HICs) serves as an effective tool for describing their dynamical evolution and exploring the properties of the strong-interacting matter produced during the collisions [1–7]. There are two main ingredients in the transport approach, i.e., the mean-field and the collision term. The former is responsible for the drift part of the transport equation, which embodies the information of the nuclear equation of state (EoS) [8–10], and the latter contains the properties of two-body scattering cross sections. By comparing the certain final-state observable obtained from the transport model with that from experimental measurements, information about the nuclear EoS can be extracted [11–19]. For example, through the observables of nuclear giant resonance [20–23], the neutron-proton flow [24–26], the nuclear stopping [27–29], the neutron-to-proton spectral ratio [30–33], and the charged pion ratio [34–36], characteristic quantities of the nuclear EoS and/or its symmetry energy term, have been extracted through studying these collisions.

The prerequisite of such a methodology is that the nucleon-nucleon (NN) cross sections in the collision term of the transport approach remain relatively fixed, or the observable shows little dependence on it. Therefore, to improve the reliability of the transport model when employing it to extract

the information of the nuclear EoS, it is necessary to narrow down the uncertainties of the NN cross sections used in transport models. Since the NN scatterings occur in the nuclear medium formed during the collisions, one should use in-medium NN cross sections σ_{NN}^* in transport models. The σ_{NN}^* is usually described by the NN cross sections in free space $\sigma_{NN}^{\text{free}}$ multiplied by a medium correction factor F , with the former being directly measured through experiments [37]. The σ_{NN}^* can be calculated using different theoretical approaches like the Dirac-Brueckner-Hartree-Fock approach and the closed time-path Green's function approach [38–42]. It is generally suppressed with respect to $\sigma_{NN}^{\text{free}}$ due to the Pauli blocking. On the other hand, the σ_{NN}^* or its correction factor F can be constrained within the transport model through experimental observables that are sensitive to the in-medium NN scatterings, such as the collective flow and the rapidity distribution [43–48]. In this case, F is usually parametrized as a function of the local density of the nuclear medium and the total kinetic energy of the two scattering nucleons [45,46]. As the total kinetic energy of the two scattering nucleons increases, the phase-space density around them decreases and the medium correction of their cross section should diminish. Therefore, observables corresponding to low energy regimes play an important role in obtaining a unified parametrization of σ_{NN}^* . The width of nuclear giant resonances Γ is related to the two-body dissipation of nucleons, which manifests itself through the NN scattering σ_{NN}^* in transport models. Consequently, the Γ provides a natural probe to study the medium effect of NN cross sections in the low-energy regime [48].

* wangrui@sinap.ac.cn

† zhangzh275@mail.sysu.edu.cn

‡ mayugang@fudan.edu.cn

In the present work, based on the Boltzmann-Uehling-Uhlenbeck (BUU) transport equation, we combine observables from nuclear stopping and that from nuclear collective motion to study the σ_{NN}^* . The lattice Hamiltonian method is employed to deal with the mean-field part of the BUU equation [49–51], while its collision integral is implemented through a full-ensemble stochastic approach [48,51–54]. Subsequently, we deduce a medium correction factor F or the σ_{NN}^* that can be used in HICs of different energy regimes. This deduction is based on experimental data from the width of the iso-vector giant dipole resonance (IVGDR) in ^{208}Pb measured through the photonuclear reaction [55,56], and the nuclear stopping data of central $^{197}\text{Au} + ^{197}\text{Au}$ collisions at an energy of 150A MeV measured by the INDRA Collaboration and the FOPI Collaboration [57–60].

The present article is organized as follows. In Sec. II, we provide the basic concepts of the BUU equation and how we solve it. Sec. III is further divided into four subsections, which cover the parametrization of the medium correction, the result of IVGDR as well as nuclear stopping based on the medium correction, and the determination of the medium correction, respectively. It includes the definition and related formulas of the observables for IVGDR and nuclear stopping, as well as the constraint of the medium correction parameters. Finally, we summarize the present work in Sec. IV.

II. MODEL DESCRIPTION

The BUU transport equation is used to describe the time evolution of the one-body phase-space distribution function of nucleons $f(\vec{r}, \vec{p})$, also known as the Wigner function. It can be derived through a semi-classical approximation to the time-dependent Hartree-Fock theory [1,61], which can be expressed as follows:

$$\frac{\partial f}{\partial t} + \frac{\vec{p}}{E} \cdot \nabla_{\vec{r}} f + \nabla_{\vec{p}} U(\vec{r}, \vec{p}) \cdot \nabla_{\vec{r}} f - \nabla_{\vec{r}} U(\vec{r}, \vec{p}) \cdot \nabla_{\vec{p}} f = I_c. \quad (1)$$

The left-hand side of Eq. (1) describes the time evolution of the $f(\vec{r}, \vec{p})$ in the momentum-dependent potential $U(\vec{r}, \vec{p})$. Meanwhile, the collision integral term I_c , which incorporates the Pauli blocking effect through the Pauli factor $(1 - f_i)$, is closely related to the σ_{NN}^* [51]. The I_c can be written

$$I_c = -g \int \frac{d^3 p_2}{(2\pi\hbar)^3} \frac{d^3 p_3}{(2\pi\hbar)^3} \frac{d^3 p_4}{(2\pi\hbar)^3} \times |\mathcal{M}_{12 \rightarrow 34}|^2 (2\pi)^4 \delta^4(p_1 + p_2 - p_3 - p_4) \times [f_2 f_3 (1 - f_4) (1 - f_1) - f_3 f_4 (1 - f_1) (1 - f_2)], \quad (2)$$

where $g = 2$ is the spin degeneracy factor and $\mathcal{M}_{12 \rightarrow 34}$ is the in-medium transition matrix element. The σ_{NN}^* can be directly introduced into I_c , through

$$\sigma_{NN}^* = \frac{1}{v_{\text{rel}}} \int \frac{d^3 p_3}{(2\pi\hbar)^3} \frac{d^3 p_4}{(2\pi\hbar)^3} |\mathcal{M}_{12 \rightarrow 34}|^2 (2\pi)^4 \times \delta^4(p_1 + p_2 - p_3 - p_4), \quad (3)$$

where v_{rel} is the relative velocity of the test nucleons. The σ_{NN}^* is usually given by multiplying the $\sigma_{NN}^{\text{free}}$ [37] by a medium correction factor F . Though omitted in Eqs. (1) and (2), the

isospin degree of freedom τ should be understood to enter those equations implicitly.

We employ the lattice Hamiltonian method [49,50] to deal with the mean-field $U(\vec{r}, \vec{p})$ evolution of the BUU equation by mimicking $f_{\tau}(\vec{r}, \vec{p}, t)$ by a large number of test nucleons [62],

$$f_{\tau}(\vec{r}, \vec{p}, t) = \frac{1}{g} \frac{(2\pi\hbar)^3}{N_E} \sum_i^{A N_E \tau} S[\vec{r}_i(t) - \vec{r}] \delta[\vec{p}_i(t) - \vec{p}]. \quad (4)$$

In the above equation, A is the mass number of the system, and N_E is the number of parallel ensembles (the number of test particles in some literature). The \vec{r}_i and \vec{p}_i correspond to the coordinates and momenta of the test nucleons, respectively. The factor S is introduced to modify the relation between test nucleons and the f , and we adopt a triangle form factor S [49,50] in the present work. The local density at a lattice site α can be obtained by the integral of the Eq. (4) concerning momentum \vec{p} ,

$$\rho_{\tau}(\vec{r}_{\alpha}, t) = g \int f_{\tau}(\vec{r}_{\alpha}, \vec{p}, t) \frac{d^3 p}{(2\pi\hbar)^3} = \frac{1}{N_E} \sum_i^{\tau} S[\vec{r}_i(t) - \vec{r}_{\alpha}], \quad (5)$$

where \vec{r}_{α} represents the coordinates of the lattice site α . The summation in the above expression runs over all test nucleons with isospin τ .

To obtain the equations of motion for the test nucleons and other physical quantities governed by the total Hamiltonian H , we need to calculate the lattice Hamiltonian H_L , which is approximately equal to the H , i.e., $H = \int \mathcal{H}(\vec{r}) d\vec{r} \approx l_x l_y l_z \sum_{\alpha} \mathcal{H}(\vec{r}_{\alpha}) \equiv H_L$. The $l_x = l_y = l_z = 0.5$ fm are the lattice spacing. Testing shows that further decreasing the lattice spacing used in the transport model has only a slight effect on the final-state observable. The Hamiltonian density \mathcal{H} is obtained from Skyrme-Hartree-Fock approach, and it contains the kinetic term, the local term, the momentum-dependent term, the density-dependent term, the gradient term, and the Coulomb term.

We employ the stochastic collision method [48,51–54] to deal with the NN scattering process within the I_c in the transport model. In the stochastic collision method, the scattering probability P_{ij} between two test nucleons i and j in a time interval Δt is a numerical value between 0 and 1, and it can be obtained directly by substituting the f in Eq. (4) into Eq. (2). It reads

$$P_{ij} = v_{\text{rel}} \sigma_{NN}^* S(\vec{r}_i - \vec{r}_{\alpha}) S(\vec{r}_j - \vec{r}_{\alpha}) l_x l_y l_z \Delta t. \quad (6)$$

Once we have determined the value of P_{ij} , it is necessary to ascertain whether a scattering between two test nucleons i and j occurs by comparing P_{ij} with a random number, which corresponds to the attempted collision. Then, we can get a true collision if this attempted collision satisfies the Pauli principle.

In the part of the initialization, the radial density distribution $\rho_{\tau}(r)$ of a ground-state nucleus is established using the Thomas-Fermi approach via the variation of the total energy E with respect to $\rho_{\tau}(r)$. The E can be defined as an integral, i.e., $E = \int \mathcal{H}[r, \rho_{\tau}(r), \nabla \rho_{\tau}(r), \nabla^2 \rho_{\tau}(r) \dots] dr$, and it is a function of $\rho_{\tau}(r)$ and its spatial gradients $\nabla^n \rho_{\tau}(r)$ [50,51]. We want to note that the Hamiltonian density \mathcal{H} used in

the initialization also governs the mean-field evolution in the BUU equation, which ensures the stability of the ground-state evolution. Based on the $\rho_\tau(r)$ we can obtain the initial coordinates \vec{r}_i of test nucleons and generate their initial momenta \vec{p}_i from a zero-temperature Fermi distribution, with local Fermi momentum defined as $p_\tau^F = \hbar[3\pi^2\rho_\tau(r)]^{1/3}$.

The present framework of solving the BUU equation is implemented numerically using high-performance parallel computing, i.e., the graphics processing unit (GPU) that enables us to employ a vast number of test particles in the calculation process, and significantly increases the numerical efficiency and accuracy [63]. More detailed descriptions of the present lattice BUU (LBUU) framework can be found in Ref. [51].

III. RESULTS AND DISCUSSION

In this work, the LBUU model is used to study the nuclear collective motion and the nuclear stopping, where we set the $N_E = 10000$ to ensure the convergence of the numerical results and select a representative Skyrme interaction SkM* [64] to simulate the NN effective interaction during these reactions. We utilize the nuclear stopping power $vartl$ and the scaled rapidity distributions in the transverse direction $Y_x = y_x/y_0$ as well as the longitudinal direction $Y_z = y_z/y_0$ of central $^{197}\text{Au} + ^{197}\text{Au}$ collisions at the energy of 150A MeV to constrain the medium correction of the σ_{NN}^* at intermediate energy. Beyond that, the width Γ of IVGDR for heavy nucleus ^{208}Pb is naturally related to the σ_{NN}^* , and it can be employed to determine the medium correction at low energy [48]. By comparing these observables obtained from the transport model with those from experimental measurement, we can extract a unified medium correction applicable to HICs across the low to intermediate energy range. For higher incident energies, the influence of the medium correction on the σ_{NN}^* in the HICs essentially disappears, i.e., the $\sigma_{NN}^{\text{free}}$ can be used directly.

A. The medium correction in the transport model

In previous studies, the medium correction can usually be obtained by the calculation based on microscopic theories and the extraction through experimental observables that are sensitive to the σ_{NN}^* [19,40–42,44,46,48,65,66]. However, some problems regarding medium correction in the low energy regime are still not completely resolved. It is found that the width Γ of nuclear collective motion is mainly composed of three parts, i.e., the escape width, the Landau damping width, and the collisional damping width [66,67]. The collisional damping is naturally related to the in-medium NN scattering in the de-excitation process of an excited nucleus and then affects the results of the Γ [48]. Therefore, we can constrain the σ_{NN}^* in low energy region using Γ of nuclear collective motion. Then considering the observables that are dependent on the σ_{NN}^* in intermediate energy collisions, we can obtain a new medium correction of the σ_{NN}^* which applies to HICs at low to intermediate energies.

The medium correction reduction factor $F = \sigma_{NN}^*/\sigma_{NN}^{\text{free}}$ is usually parametrized to depend on both the local nucleon density and the total kinetic energy of the two scattering

nucleons. Since the medium correction is mainly a consequence of the Pauli blocking caused by the nucleons in the nuclear medium, the F should approach 1.0 when the local nucleon density decreases or the total kinetic energy increases. We choose an exponential reduction factor, which has been used to parametrize the medium correction factor of the NN cross sections calculated from the T -matrix approach [40,41]. The in-medium NN cross sections used in the present work read

$$\begin{aligned}\sigma_{nn}^* &= \sigma_{nn}^{\text{free}} \exp \left[-\alpha_{nn} \frac{\left(\frac{2\rho_n}{\rho_0}\right)^{1/3}}{1 + \left(\frac{T_{c.m.}}{0.015 \text{ GeV}}\right)^3} \right], \\ \sigma_{np}^* &= \sigma_{np}^{\text{free}} \exp \left[-\alpha_{np} \frac{\left(\frac{\rho_n + \rho_p}{\rho_0}\right)^{1/3}}{1 + \left(\frac{T_{c.m.}}{0.045 \text{ GeV}}\right)} \right].\end{aligned}\quad (7)$$

In the above equations, the σ_{nn}^* represents the in-medium cross sections of the elastic scattering channels $n + n \rightarrow n + n$ or $p + p \rightarrow p + p$, while the σ_{np}^* being the cross section of the elastic scattering channel of $n + p \rightarrow n + p$. Here, we focus solely on NN elastic scattering. The local neutron (proton) density ρ_n and ρ_p during the evolution of HICs can be calculated through Eq. (5), where the $\rho_0 = 0.16 \text{ fm}^{-3}$ represents the nuclear normal density. The $T_{c.m.}$ is the total kinetic energy of two scattering nucleons in the rest frame of the local medium. In the following Secs. III B, III C, and III D, we provide a detailed discussion of using the LBUU model with Eq. (7) to calculate the IVGDR and the nuclear stopping, as well as the process of constraining the values of the medium correction parameters α_{nn} and α_{np} .

B. In-medium NN elastic cross section and nuclear giant dipole resonance

Typically, the nuclear collective motion can be generated by acting as a perturbation excitation operator \hat{Q} on the ground-state Hamiltonian \hat{H}_0 at the initial time t_0 , i.e., $\hat{H}(t) = \hat{H}_0 + \lambda \hat{Q} \delta(t - t_0)$, where the λ is a small excitation parameter and the $\delta(t - t_0)$ is the Dirac delta function. The expectation value of the excitation operator $\langle \hat{Q} \rangle$ is the key quantity used to study the collective motion of a nucleus. For a nucleus consisting of A nucleons (comprising N neutrons and Z protons), $\langle \hat{Q} \rangle$ can be expressed through the Wigner function $f(\vec{r}, \vec{p})$ in the Wigner representation [61,68]

$$\langle \hat{Q} \rangle = \int f(\vec{r}, \vec{p}) q(\vec{r}, \vec{p}) d^3\vec{r} d^3\vec{p}. \quad (8)$$

In Eq. (8), the $q(\vec{r}, \vec{p})$ represents the Wigner transform of single-nucleon excitation operator \hat{q}_i acting on each nucleon, with the latter connected to the single-particle excitation operator \hat{Q} through $\hat{Q} = \sum_i^A \hat{q}_i$. For the IVGDR, the excitation operator \hat{Q}_{IVD} can be written as

$$\hat{Q}_{\text{IVD}} = \frac{N}{A} \sum_{i=1}^Z \hat{z}_i - \frac{Z}{A} \sum_{i=1}^N \hat{z}_i, \quad (9)$$

where \hat{z}_i is the z -axis component of the coordinate operator of the i th nucleon. The detailed derivation of the relevant equations can be found in Refs. [23,50,51]. Transport models

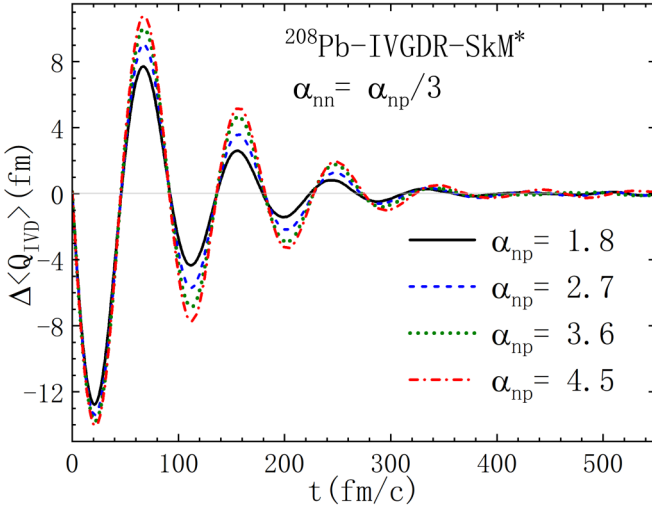


FIG. 1. The time evolution of $\Delta\langle\hat{Q}_{IVD}\rangle$ in ^{208}Pb from LBUU calculations using various values of α_{np} and α_{nn} .

have been employed extensively to study the nuclear giant resonances [21,69–73].

The collectively excited nucleus can be obtained by changing the initial coordinates \vec{r}_i and momenta \vec{p}_i of each test nucleon from the ground-state nucleus according to the form of the external excitation operator in the transport model. For the dipole-excited nucleus, we only need to modify the initial momenta of test nucleons through

$$p_{zi} \rightarrow \begin{cases} p_{zi} - \lambda \frac{N}{A} & \text{for protons,} \\ p_{zi} + \lambda \frac{Z}{A} & \text{for neutrons,} \end{cases} \quad (10)$$

where the p_{zi} is the component of the momentum of the i th nucleon along the z axis. We set the excitation parameter λ to be 0.015 GeV/c in the present work.

After exciting the nucleus based on Eq. (10), we can get a dipole-excited nucleus and its time evolution of the $\langle\hat{Q}\rangle(t)$. Subsequently, we can obtain the strength function $S(E)$ based on the Fourier integral of $\Delta\langle\hat{Q}\rangle(t)$ in the linear response theory [74],

$$S(E) = -\frac{1}{\pi\lambda} \int_0^\infty dt \Delta\langle\hat{Q}\rangle(t) \sin \frac{Et}{\hbar}. \quad (11)$$

The $\Delta\langle\hat{Q}\rangle(t) = \langle 0' | \hat{Q} | 0' \rangle - \langle 0 | \hat{Q} | 0 \rangle$ represents the time evolution of the response function of the nucleus to the \hat{Q} , with $|0\rangle$ and $|0'\rangle$ denoting the nuclear states before and after the perturbation, respectively [51]. It is worth noting that the full width at half-maximum Γ of the $S(E)$ is related to the σ_{NN}^* and can be adopted to determine the medium correction in low energy. We can employ the experimental $\Gamma_{\text{exp.}}$ of the IVGDR presented in Ref. [56] to constrain the σ_{NN}^* within the transport model, thereby determining an appropriate medium correction in low-energy.

As shown in Fig. 1, we first calculate the time evolution of the $\Delta\langle\hat{Q}_{IVD}\rangle$ in ^{208}Pb based on LBUU model. The black solid line, the blue dashed line, the green dotted line, and the red dash-dotted line represent the result based on the different values of α_{np} and α_{nn} in Eq. (7), respectively. We notice from

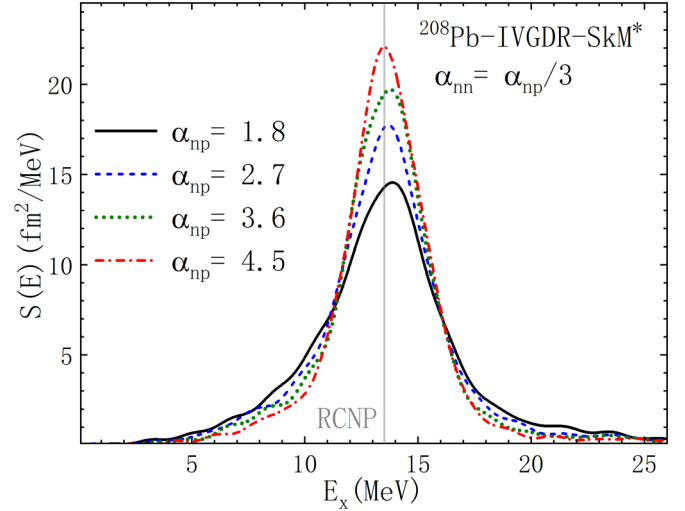


FIG. 2. The $S(E)$ of the IVGDR in ^{208}Pb with different values of α_{np} and α_{nn} . The gray solid line represents the experimental excitation energy $E_x = 13.4$ MeV [55].

the figure that the result represented through the black solid line, with the $\alpha_{np} = 1.8$ ($\alpha_{nn} = 0.6$), exhibits the least oscillation among the four cases, indicating the strongest damping. On the contrary, the maximum oscillation and the weakest damping occur in the results represented through the red dash-dotted line, with the $\alpha_{np} = 4.5$ ($\alpha_{nn} = 1.5$). The damping of the nuclear collective motion, reflecting the restraining capability for NN scattering by dissipation of energy, is directly related to the σ_{NN}^* and subsequently influences the Γ of the $S(E)$. Therefore, the IVGDR with the $\alpha_{np} = 1.8$ ($\alpha_{nn} = 0.6$) in Fig. 1 should have a weakest damping and a largest Γ .

In Fig. 2, the strength function $S(E)$ of the IVGDR in ^{208}Pb is calculated with the Fourier integral based on results shown in Fig. 1, and the legends of lines are the same as Fig. 1. As the α_{np} and the α_{nn} increases, the Γ of the $S(E)$, connecting with the σ_{NN}^* , have an obvious tendency to decrease corresponding to the property of the damping. This trend allows us to find the correlation between the Γ of the IVGDR and the medium correction. The gray solid line represents the experimental excitation energy $E_x = 13.4$ MeV of the $S(E)$ measured at RCNP [55]. Interestingly, the $S(E)$ obtained through different α_{np} and α_{nn} give similar E_x . This suggests that the σ_{NN}^* has little effect on the E_x . Similar results on the isoscalar giant quadrupole resonance have been observed in Ref. [23].

In order to visualize the correlation between the Γ of the IVGDR in ^{208}Pb and the medium correction, we show the Γ calculated through the LBUU model with different α_{np} and α_{nn} in Fig. 3. The gray hatched band corresponds to the experimental width $\Gamma_{\text{exp}} = 4.08 \pm 0.09$ MeV [56]. First, we explore the influence of α_{nn} on the Γ and conduct a detailed analysis by varying the value of α_{nn} from 0.3 to 3.0 while keeping α_{np} constant at 3.0. The inset of Fig. 3 demonstrates that results for different α_{nn} (the green empty circle) oscillate in small amplitude around the $\Gamma_{\text{exp.}}$, i.e., α_{nn} having almost no influence on the Γ . Therefore, in the following discussion, we pay more attention to the constraint on the parameter α_{np} and fix the value of $\alpha_{nn} = \alpha_{np}/3$. In Fig. 3, the red solid circles

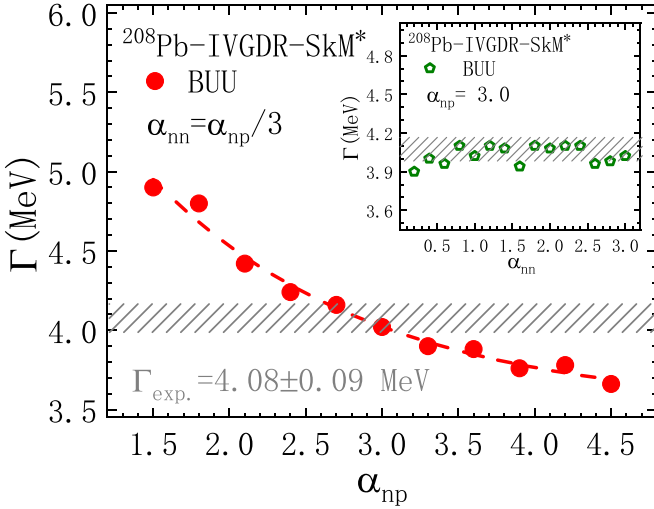


FIG. 3. The correlation between the α_{np} (α_{nn}) and the Γ of the IVGDR in ^{208}Pb . The red solid circles are results based on different α_{np} ($\alpha_{nn} = \alpha_{np}/3$) with the LBUU model, and the green empty circles in the inset are results based on different α_{nn} ($\alpha_{np} = 3.0$). The gray hatched band corresponds to the experimental width $\Gamma_{\text{exp}} = 4.08 \pm 0.09$ MeV [56].

and the red dashed line represent the results obtained from the LBUU model and its fitting line, respectively. It is evident that the tendency of the Γ decreases from 4.90 MeV to 3.65 MeV with the increase of α_{np} , and it reproduces well the Γ_{exp} of the IVGDR in ^{208}Pb when selecting parameters near the $\alpha_{np} = 3.0$ ($\alpha_{nn} = 1.0$).

C. In-medium NN elastic scattering cross section and nuclear stopping

The nuclear stopping power vartl , first proposed by the FOPI Collaboration, is one of the essential observables for understanding the basic reaction dynamics in the HICs, and it can be used to directly reflect the degree of stopping of the projectile [57,75,76]. The vartl refers to the ratio of the variances of the rapidity distributions in the transverse direction and the longitudinal direction of the emitted particles in the HICs, defined as $\text{vartl} = \langle y_x^2 \rangle / \langle y_z^2 \rangle$ [57,59]. When the $\langle y_x^2 \rangle$ and the $\langle y_z^2 \rangle$ are approximately equal, i.e., $\text{vartl} \approx 1$, it indicates that the projectile is theoretically completely stopped by the target.

Based on the results from the FOPI and INDRA Collaboration [58,59,77], the experimental vartl of light-charged particles ($Z = 1$) in the central $^{197}\text{Au} + ^{197}\text{Au}$ collisions at the energy of 150A MeV and the impact parameter $b \leq 2$ fm is estimated to be $\text{vartl}_{\text{exp}} = 0.85 \pm 0.05$. With the proton number of the emitted particles increasing steadily to 20, the value of $\text{vartl}_{\text{exp}}$ is reduced to around 0.1. This indicates that the type of the emitted particles included in the calculation of vartl can significantly affect the results. Therefore, we only compare the calculated proton vartl with the experimental measurement for light-charged nuclei ($Z = 1$).

In Fig. 4, we display the proton vartl (the black solid circles) for central $^{197}\text{Au} + ^{197}\text{Au}$ collisions at the incident

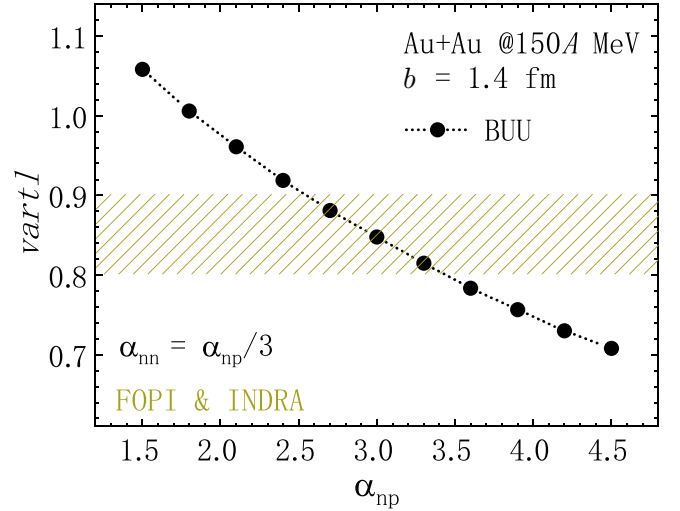


FIG. 4. The proton vartl for central Au + Au collisions at the energy of 150A MeV and the impact parameter of $b = 1.4$ fm calculated using the LBUU model as a function of the α_{np} . The brown hatched band corresponds to the measured $\text{vartl}_{\text{exp}} = 0.85 \pm 0.05$ for $Z = 1$ particles in central collisions of $b \leq 2$ fm by the FOPI and INDRA Collaborations [59].

energy of 150A MeV and the impact parameter $b = 1.4$ fm based on the LBUU model with the Skyrme interaction SkM* and various values of α_{np} (α_{nn}). Here, we still set $\alpha_{nn} = \alpha_{np}/3$. For comparison, we show the experimental $\text{vartl}_{\text{exp}} = 0.85 \pm 0.05$ for $Z = 1$ particles in the central $^{197}\text{Au} + ^{197}\text{Au}$ collisions at the energy of 150A MeV and the impact parameter of $b \leq 2$ fm through the hatched band [59]. As expected, a larger α_{np} leads to smaller in-medium NN cross sections and thus a smaller vartl value. And it is seen that with the α_{np} in the range of 2.7–3.3, the LBUU results are in good agreement with the experimental measurements.

With the INDRA 4π multidetector, the central 150A MeV $^{197}\text{Au} + ^{197}\text{Au}$ collisions have been measured well at centrality 0–2% [59]. In these reactions, the scaled rapidity distributions in the longitudinal direction $Y_z = y_z/y_0$ and the transverse direction $Y_x = y_x/y_0$ for several fragment species with charge numbers Z ranging from 1 to 20 can also be utilized to constrain the σ_{NN}^* in intermediate energy. The y_0 is the beam rapidity in the center-of-mass frame. The y_z and y_x are defined as

$$\begin{aligned} y_z &= \frac{1}{2} \ln \frac{E + p_z}{E - p_z}, \\ y_x &= \frac{1}{2} \ln \frac{E + p_x}{E - p_x}, \end{aligned} \quad (12)$$

where the p_z and p_x represent the momentum of the particle along the Z axis and X axis, respectively, and $E = \sqrt{m^2 + p^2}$ is the nucleon energy. To further study the effect of the medium correction in intermediate energy, we simulate the central $^{197}\text{Au} + ^{197}\text{Au}$ collisions at the energy of 150A MeV and impact parameter $b = 1.4$ fm through the LBUU model with different parameters α_{np} to extract the results of the Y_z and Y_x . It should be noted that, since the experimental transverse rapidity distribution is in an arbitrarily fixed transverse

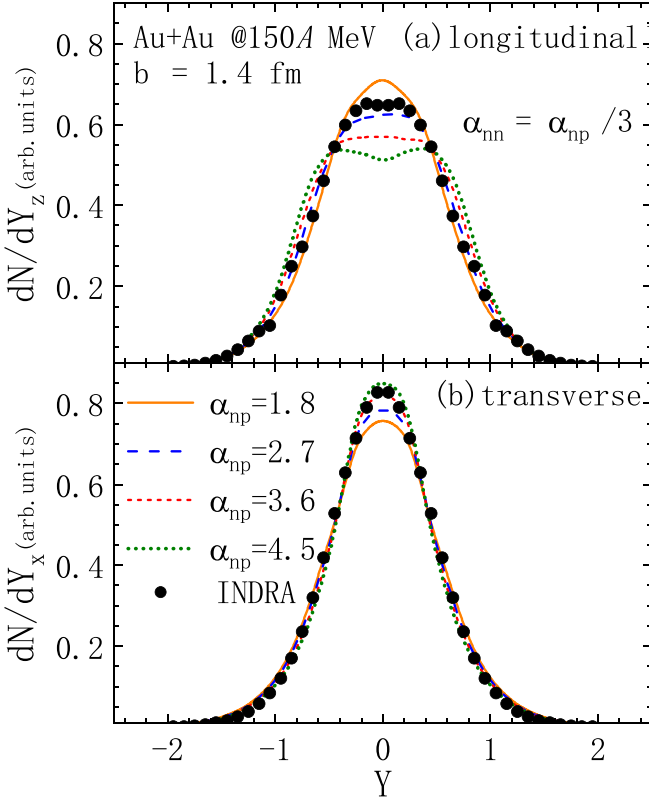


FIG. 5. The scaled proton longitudinal (upper panel) and transverse (lower panel) rapidity distributions for central Au + Au collisions at the energy of 150A MeV and the impact parameter of $b = 1.4$ fm calculated using the LBUU model with four values of the α_{np} . The coalescence invariant proton rapidity distributions measured by the INDRA collaboration [59] are shown as black solid circles. All distributions are normalized for a easier comparison of their shape.

direction [59], the calculated dN/dY_x is obtained by averaging the rapidity distribution in x and y directions from LBUU simulations.

The scaled rapidity distributions in the longitudinal and the transverse direction obtained from the LBUU model, are compared with experimental measurements in Figs. 5(a) and 5(b), respectively. The yellow solid lines, the blue dashed lines, the red dotted lines, and the green short dotted lines represent the results of scaled rapidity distributions for proton, obtained by varying the $\alpha_{np} = 1.8$ to $\alpha_{np} = 4.5$, using the LBUU model with the Skyrme interaction SkM*. In the center-of-mass frame of the colliding system, these rapidities are calculated through the information of the protons in the phase-space of $t = 300$ fm/c. The black solid circles represent the experimental coalescence invariant proton rapidity distributions which are given by the sum of measured rapidity distributions of all charged baryonic particles with $Z \leq 20$ weighted with their respective charges. For easier comparison, both theoretical and experimental spectra are normalized by their respective total charged numbers. According to our transport calculation, the neutron and proton density can reach as high as $\rho_n = 0.156$ and $\rho_p = 0.097$, respectively, in the central $5 \times 5 \times 5$ fm³ area of the reaction region. This enables

us to explore the high-density behavior of σ_{NN}^* shown in Eq. (7).

As can be seen from Fig. 5, with the α_{np} increasing, the scaled longitudinal (transverse) rapidity distribution becomes wider (narrower), and its maximum value decreases (increases), because a larger α_{np} leads to a smaller σ_{NN}^* and thus results in weaker nuclear stopping. Particularly, one can see that, compared with the transverse rapidity distribution, the longitudinal one is much more sensitive to the α_{np} , which suggests that the dN/dY_z should be a better probe of the σ_{NN}^* . Further comparing the LBUU results with the experimental coalescence invariant proton rapidity distributions, we find the INDRA data for dN/dY_z favors $\alpha_{np} = 2.4$, while those for dN/dY_x prefers a larger value of $\alpha_{np} = 3.9$. Similar with the Γ of IVGDR, we find that the results of $vartl$ and scaled rapidity distributions based on the LBUU model are not sensitive to the parameter α_{nn} . Therefore, we adopt the parameter $\alpha_{nn} = \alpha_{np}/3$ in Eq. (7), and only focus on the constraint on the value of α_{np} in the next subsection.

D. Determination of the in-medium correction parameter α_{np}

Given the sensitivities of the IVGDR width, the $vartl$, and the scaled longitudinal and transverse rapidity distributions to the σ_{NN}^* as demonstrated in previous sections, we further determine the medium correction parameter α_{np} in Eq. (7) by minimizing the sum of the squared deviations from the data [78],

$$\chi^2 = \sum_{i=1}^{N_d} \frac{[\mathcal{O}_i(\alpha_{np}) - \mathcal{O}_i^{\text{exp}}]^2}{\Delta \mathcal{O}_i}. \quad (13)$$

Here, $\mathcal{O}_i^{\text{exp}}$ stands for experimental data for the i th selected observables, \mathcal{O}_i represents the calculated values, and $\Delta \mathcal{O}_i$ is the adopted error. In this work, we take into account four experimental data including the IVGDR width of ²⁰⁸Pb, the $vartl$ of $Z = 1$ particles, and the coalescence invariant proton dN/dY_z and dN/dY_x at $Y = 0.05$. The adopted errors for the IVGDR width of ²⁰⁸Pb and the $vartl$ in central ¹⁹⁷Au + ¹⁹⁷Au collisions are taken to be the experimental uncertainties of $\sigma_T = 0.09$ MeV and $\sigma_{vartl} = 0.05$, respectively. As to the scaled longitudinal and transverse rapidity distributions, since their experimental uncertainties are not given in Ref. [59], we tune their adopted errors following the usual strategy [78], to guarantee the minimum of total χ^2 is around the degree of freedom (3 in our case) and their weights are similar. The resulting adopted errors for the scaled longitudinal and transverse direction are $\sigma_{dN/dY_z} = 0.03$ and $\sigma_{dN/dY_x} = 0.03$, respectively.

The obtained χ^2 as a function of the medium correction parameter α_{np} is shown in Fig. 6, the χ_i^2 for the IVGDR width, the $vartl$, the dN/dY_z and dN/dY_x contained in χ^2 per data point are also shown as blue circles, the red squares, the green stars, and the orange triangles in the inset of Fig. 6, respectively. The χ_i^2 represent single observation's contribution to the χ^2 under each type and indicate their sensitivity to parameters α_{np} . It is seen that the IVGDR width, the $vartl$, the dN/dY_z , and dN/dY_x data prefer 3.0, 3.0, 2.4, and 3.9, respectively, where the χ_{dN/dY_x}^2 (χ_{GDR}^2) makes a relatively smaller (larger) contribution to calculating χ^2 . By combining

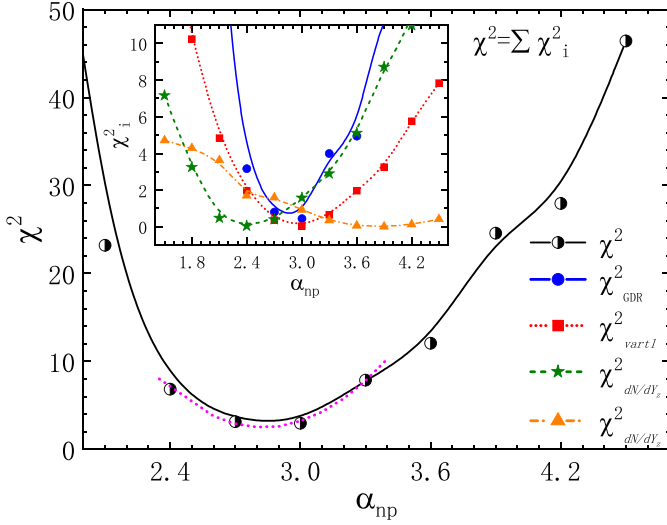


FIG. 6. χ^2 as a function of the medium correction parameter α_{np} . The contributions on the χ^2 from the IVGDR width, the $var1$, and the coalescence invariant proton longitudinal and transverse rapidity distributions, i.e., χ_{GDR}^2 , χ_{var1}^2 , $\chi_{dN/dY}^2$, and $\chi_{dN/dY}^2$ are shown as the blue circles, red squares, green stars, and orange triangles in the inset, respectively.

all these data and employing a parabolic fit of the results of $2.4 \leq \alpha_{np} \leq 3.3$ (magenta dotted line), we determine the medium correction parameter α_{np} with the minimum χ^2 to be 2.8.

In Fig. 7, we show the total kinetic energy $T_{c.m.}$ dependence of the medium correction $\sigma_{NN}^*/\sigma_{NN}^{free}$ at different local densities ρ . The results of Figs. 7(a), 7(b), and 7(c) are based on the $\rho = 0.01 \text{ fm}^{-3}$, $\rho = 0.05 \text{ fm}^{-3}$, and $\rho = 0.16 \text{ fm}^{-3}$, respectively. The black solid line and the red dashed line are the $\sigma_{NN}^*/\sigma_{NN}^{free}$ of the elastic scattering channel with $\alpha_{np} = 2.8$ and $\alpha_{nn} = \alpha_{np}/3$ in Eq. (7). The green dotted line is the $\sigma_{NN}^*/\sigma_{NN}^{free}$ obtained solely from the IVGDR width of ^{208}Pb in Ref. [48]. By comparing the results at different local densities, it can be found that both two medium corrections have more suppression for the σ_{NN}^* in low energy region, and it gradually disappears when the ρ decreases or the $T_{c.m.}$ increases. The suppression for the σ_{NN}^* of the green dotted line has a large change in different ρ , and it means that the medium correction in Ref. [48] is more sensitive to the local density. In contrast, the cases of the black solid line and the red dashed line are less affected by the changes of the ρ .

IV. SUMMARY

In the present study, the $\sigma_{NN}^*/\sigma_{NN}^{free}$ has been investigated through the IVGDR and the nuclear stopping with the LBUU model. We employ a lattice Hamiltonian method based on the Skyrme-Hartree-Fock approach, to solve accurately and

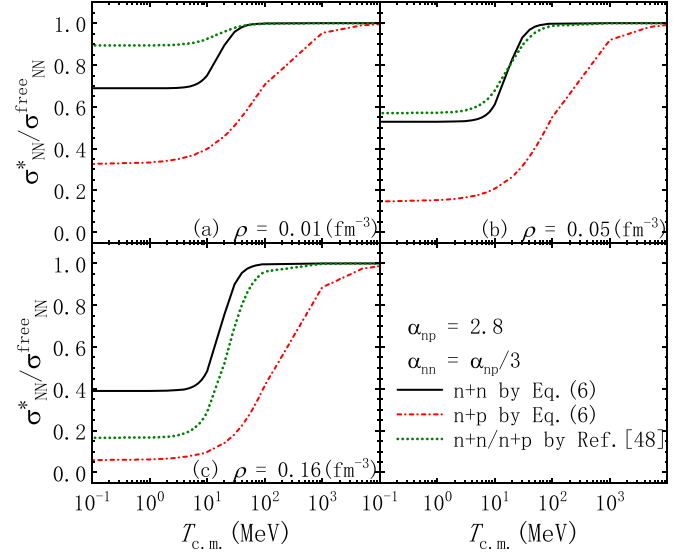


FIG. 7. The $T_{c.m.}$ dependence of the medium correction at different local density $\rho_n = \rho_p = \rho/2$. The black solid line and the red dashed line are calculated through Eq. (7) with $\alpha_{np} = 2.8$. The green dotted line is the result of the medium correction in Ref. [48].

efficiently the BUU equation with the use of a sufficiently large number of test particles. Based on the experimental observables that are sensitive to σ_{NN}^* , e.g., the Γ of the IVGDR in ^{208}Pb , the $var1$ and the scaled rapidity distributions for central $^{197}\text{Au} + ^{197}\text{Au}$ collisions at the energy of 150A MeV, we extract the in-medium NN cross sections σ_{NN}^* that can be applied to the HICs from low energy to intermediate energy. It will reduce the uncertainties of the BUU equation when applying it to nuclear collective motion and heavy-ion collisions to extract the information of the nuclear equation of state. It will also be helpful for the experimental research of the dipole excitation of nuclei in the future, e.g., at the facility of Shanghai Laser-electron gamma source (SLEGS) [79–81].

ACKNOWLEDGMENTS

We thank Chen Zhong for setting up and maintaining the GPU server, and Jaroslaw Łukasik for providing us the INDRA data on scaled rapidity distributions of central $^{197}\text{Au} + ^{197}\text{Au}$ collisions at the energy of 150A MeV. This work is partially supported by the National Natural Science Foundation of China under Contracts No. 11890714, No. 11891070, No. 12147101, No. 11905302, No. 12235010, the Guangdong Major Project of Basic and Applied Basic Research No. 2020B0301030008, and the Key Research Program of the CAS under Grant No. XDB34000000.

- [1] G. F. Bertsch and S. Das Gupta, A guide to microscopic models for intermediate energy heavy-ion collisions, *Phys. Rep.* **160**, 189 (1988).
- [2] J. Aichelin, “Quantum” molecular dynamics - A dynamical microscopic n-body approach to investigate fragment formation

and the nuclear equation of state in heavy ion collisions, *Phys. Rep.* **202**, 233 (1991).

- [3] J. Xu, L. W. Chen, M. B. Tsang, H. Wolter, Y. X. Zhang, J. Aichelin, M. Colonna, D. Cozma, P. Danielewicz, Z. Q. Feng, A. LeFevre, T. Gaitanos, C. Hartnack, K. Kim, Y. Kim,

- C. M. Ko, B. A. Li, Q. F. Li, Z. X. Li, P. Napolitani, A. Ono, M. Papa, T. Song, J. Su, J. L. Tian, N. Wang, Y. J. Wang, J. Weil, W. J. Xie, F. S. Zhang, and G. Q. Zhang, Understanding transport simulations of heavy-ion collisions at 100A and 400A MeV: Comparison of heavy-ion transport codes under controlled conditions, *Phys. Rev. C* **93**, 044609 (2016).
- [4] Y. X. Zhang, Y. J. Wang, M. Colonna *et al.*, Comparison of heavy-ion transport simulations: Collision integral in a box, *Phys. Rev. C* **97**, 034625 (2018).
- [5] A. Ono, J. Xu, M. Colonna *et al.*, Comparison of heavy-ion transport simulations: Collision integral with pions and Δ resonances in a box, *Phys. Rev. C* **100**, 044617 (2019).
- [6] M. Colonna, Y. X. Zhang, Y. J. Wang *et al.*, Comparison of heavy-ion transport simulations: Mean-field dynamics in a box, *Phys. Rev. C* **104**, 024603 (2021).
- [7] H. Wolter, M. Colonna, D. Cozma *et al.*, Transport model comparison studies of intermediate-energy heavy-ion collisions, *Prog. Part. Nucl. Phys.* **125**, 103962 (2022).
- [8] L. W. Chen, B. J. Cai, C. M. Ko *et al.*, Higher-order effects on the incompressibility of isospin asymmetric nuclear matter, *Phys. Rev. C* **80**, 014322 (2009).
- [9] C. Fuchs and H. H. Wolter, Modelization of the EOS, *Eur. Phys. J. A* **30**, 5 (2006).
- [10] M. Oertel, M. Hempel, T. Klöhn *et al.*, Equations of state for supernovae and compact stars, *Rev. Mod. Phys.* **89**, 015007 (2017).
- [11] P. Danielewicz, R. Lacey, and W. G. Lynch, Determination of the equation of state of dense matter, *Science* **298**, 1592 (2002).
- [12] B. A. Li, L. W. Chen, and C. M. Ko, Recent progress and new challenges in isospin physics with heavy-ion reactions, *Phys. Rep.* **464**, 113 (2008).
- [13] B. G. Todd-Rutel and J. Piekarewicz, Neutron-rich nuclei and neutron stars: A new accurately calibrated interaction for the study of neutron-rich matter, *Phys. Rev. Lett.* **95**, 122501 (2005).
- [14] Y. T. Cao, X. G. Deng, and Y. G. Ma, Impact of magnetic field on the giant dipole resonance of ^{40}Ca using an extended quantum molecular dynamics model, *Phys. Rev. C* **106**, 014611 (2022).
- [15] P. C. Li, Y. J. Wang, Q. F. Li *et al.*, Transport model analysis of the pion interferometry in Au + Au collisions at $E_{\text{beam}} = 1.23$ GeV/nucleon, *Sci. China Phys. Mech. Astron.* **66**, 222011 (2023).
- [16] P. C. Li, J. Steinheimer, T. Reichert *et al.*, Effects of a phase transition on two-pion interferometry in heavy ion collisions at $\sqrt{s_{NN}} = 2.4\text{--}7.7$ GeV, *Sci. China Phys. Mech. Astron.* **66**, 232011 (2023).
- [17] J. F. Xu, C. J. Xia, Z. Y. Lu *et al.*, Symmetry energy of strange quark matter and tidal deformability of strange quark stars, *Nuclear Science and Techniques* **33**, 143 (2022).
- [18] J. Liu, C. Gao, N. Wan, and C. Xu, Basic quantities of the equation of state in isospin asymmetric nuclear matter, *Nucl. Sci. Tech.* **32**, 117 (2021).
- [19] D. D. S. Coupland, W. G. Lynch, M. B. Tsang, P. Danielewicz, and Y. Zhang, Influence of transport variables on isospin transport ratios, *Phys. Rev. C* **84**, 054603 (2011).
- [20] C. Tao, Y. G. Ma, G. Q. Zhang, X. G. Cao, D. Q. Fang, and H. W. Wang, Pygmy and giant dipole resonances by coulomb excitation using a quantum molecular dynamics model, *Phys. Rev. C* **87**, 014621 (2013).
- [21] H. Y. Kong, J. Xu, L. W. Chen, B. A. Li, and Y. G. Ma, Constraining simultaneously nuclear symmetry energy and neutron-proton effective mass splitting with nucleus giant resonances using a dynamical approach, *Phys. Rev. C* **95**, 034324 (2017).
- [22] J. Xu and W. T. Qin, Nucleus giant resonances from an improved isospin-dependent Boltzmann-Uehling-Uhlenbeck transport approach, *Phys. Rev. C* **102**, 024306 (2020).
- [23] Y. D. Song, R. Wang, Z. Zhang, and Y. G. Ma, Nuclear giant quadruple resonance within a transport approach and its constraint on the nucleon effective mass, *Phys. Rev. C* **104**, 044603 (2021).
- [24] B. A. Li, Neutron-proton differential flow as a probe of isospin-dependence of the nuclear equation of state, *Phys. Rev. Lett.* **85**, 4221 (2000).
- [25] Y. Gao, G. C. Yong, L. Zhang, and W. Zuo, Influence of the nuclear symmetry energy on the collective flows of charged pions, *Phys. Rev. C* **97**, 014609 (2018).
- [26] W. J. Xie and F.-S. Zhang, Nuclear collective flows as a probe to the neutron-proton effective mass splitting, *Phys. Lett. B* **735**, 250 (2014).
- [27] S. Kumar, S. Kumar, and R. K. Puri, Effect of the symmetry energy on nuclear stopping and its relation to the production of light charged fragments, *Phys. Rev. C* **81**, 014601 (2010).
- [28] F. Fu, Z. G. Xiao, Y. P. Zhang *et al.*, Nuclear stopping and compression in heavy-ion collisions at intermediate energies, *Phys. Lett. B* **666**, 359 (2008).
- [29] F. Zhang and J. Su, Probing neutron-proton effective mass splitting using nuclear stopping and isospin mix in heavy-ion collisions in GeV energy region, *Nucl. Sci. Tech.* **31**, 77 (2020).
- [30] M. A. Famiano, T. Liu, W. G. Lynch *et al.*, Neutron and proton transverse emission ratio measurements and the density dependence of the asymmetry term of the nuclear equation of state, *Phys. Rev. Lett.* **97**, 052701 (2006).
- [31] M. B. Tsang, Y. X. Zhang, P. Danielewicz, M. Famiano, Z. Li, W. G. Lynch, and A. W. Steiner, Constraints on the density dependence of the symmetry energy, *Phys. Rev. Lett.* **102**, 122701 (2009).
- [32] D. D. S. Coupland, M. Youngs, Z. Chajecski, W. G. Lynch, M. B. Tsang, Y. X. Zhang, M. A. Famiano, T. K. Ghosh, B. Giacherio, M. A. Kilburn, J. Lee, H. Liu, F. Lu, P. Morfouace, P. Russotto, A. Sanetullaev, R. H. Showalter, G. Verde, and J. Winkelbauer, Probing effective nucleon masses with heavy-ion collisions, *Phys. Rev. C* **94**, 011601(R) (2016).
- [33] P. Morfouace, C. Y. Tsang, Y. Zhang *et al.*, Constraining the symmetry energy with heavy-ion collisions and Bayesian analyses, *Phys. Lett. B* **799**, 135045 (2019).
- [34] Z. G. Xiao, B. A. Li, L. W. Chen, G. C. Yong, and M. Zhang, Circumstantial evidence for a soft nuclear symmetry energy at suprasaturation densities, *Phys. Rev. Lett.* **102**, 062502 (2009).
- [35] Z. Q. Feng and G. M. Jin, Probing high-density behavior of symmetry energy from pion emission in heavy-ion collisions, *Phys. Lett. B* **683**, 140 (2010).
- [36] J. Estee, W. G. Lynch, C. Y. Tsang *et al.*, Probing the symmetry energy with the spectral pion ratio, *Phys. Rev. Lett.* **126**, 162701 (2021).
- [37] J. Cugnon, D. L'Hôte, and J. Vandermeulen, Simple parametrization of cross-sections for nuclear transport studies up to the GeV range, *Nucl. Instrum. Methods Phys. Res. B* **111**, 215 (1996).

- [38] G. Q. Li and R. Machleidt, Microscopic calculation of in-medium nucleon-nucleon cross sections, *Phys. Rev. C* **48**, 1702 (1993).
- [39] G. Q. Li and R. Machleidt, Microscopic calculation of in-medium proton-proton cross sections, *Phys. Rev. C* **49**, 566 (1994).
- [40] C. Fuchs, A. Faessler, and M. El-Shabshiry, Off-shell behavior of the in-medium nucleon-nucleon cross section, *Phys. Rev. C* **64**, 024003 (2001).
- [41] T. Alm, G. Röpke, and M. Schmidt, Critical enhancement of the in-medium nucleon-nucleon cross section at low temperatures, *Phys. Rev. C* **50**, 31 (1994).
- [42] F. Sammarruca and P. Krastev, Effective nucleon-nucleon cross sections in symmetric and asymmetric nuclear matter, *Phys. Rev. C* **73**, 014001 (2006).
- [43] Y. X. Zhang, Z. X. Li, and P. Danielewicz, In-medium NN cross sections determined from the nuclear stopping and collective flow in heavy-ion collisions at intermediate energies, *Phys. Rev. C* **75**, 034615 (2007).
- [44] O. Lopez, D. Durand, G. Lehaut *et al.*, In-medium effects for nuclear matter in the Fermi-energy domain, *Phys. Rev. C* **90**, 064602 (2014).
- [45] B. Barker and P. Danielewicz, Shear viscosity from nuclear stopping, *Phys. Rev. C* **99**, 034607 (2019).
- [46] L. Ou and X. Y. He, In-medium nucleon-nucleon elastic cross-sections determined from the nucleon induced reaction cross-section data, *Chin. Phys. C* **43**, 044103 (2019).
- [47] P. C. Li, Y. J. Wang, Q. F. Li *et al.*, Accessing the in-medium effects on nucleon-nucleon elastic cross section with collective flows and nuclear stopping, *Phys. Lett. B* **828**, 137019 (2022).
- [48] R. Wang, Z. Zhang, L. W. Chen *et al.*, Constraining the in-medium nucleon-nucleon cross section from the width of nuclear giant dipole resonance, *Phys. Lett. B* **807**, 135532 (2020).
- [49] R. J. Lenk and V. R. Pandharipande, Nuclear mean field dynamics in the lattice Hamiltonian Vlasov method, *Phys. Rev. C* **39**, 2242 (1989).
- [50] R. Wang, L. W. Chen, and Z. Zhang, Nuclear collective dynamics in the lattice Hamiltonian Vlasov method, *Phys. Rev. C* **99**, 044609 (2019).
- [51] R. Wang, Z. Zhang, L. W. Chen *et al.*, Nuclear collective dynamics in transport model with the lattice Hamiltonian method, *Frontiers in Physics* **8**, 330 (2020).
- [52] P. Danielewicz and G. F. Bertsch, Production of deuterons and pions in a transport model of energetic heavy-ion reactions, *Nucl. Phys. A* **533**, 712 (1991).
- [53] Z. Xu and C. Greiner, Thermalization of gluons in ultrarelativistic heavy ion collisions by including three-body interactions in a parton cascade, *Phys. Rev. C* **71**, 064901 (2005).
- [54] R. Wang, Y. G. Ma, L. W. Chen, C. M. Ko, K. J. Sun, and Z. Zhang, Kinetic approach of light-nuclei production in intermediate-energy heavy-ion collisions, *Phys. Rev. C* **108**, L031601 (2023).
- [55] A. Tamii, I. Poltoratska, P. von Neumann-Cosel *et al.*, Complete electric dipole response and the neutron skin in ^{208}Pb , *Phys. Rev. Lett.* **107**, 062502 (2011).
- [56] V. A. Plujko, O. M. Gorbachenko, R. Capote *et al.*, Giant dipole resonance parameters of ground-state photoabsorption: Experimental values with uncertainties, *At. Data Nucl. Data Tables* **123–124**, 1 (2018).
- [57] W. Reisdorf, A. Andronic, A. Gobbi *et al.*, Nuclear stopping from 0.09A to 1.93A GeV and its correlation to flow, *Phys. Rev. Lett.* **92**, 232301 (2004).
- [58] J. Łukasik, G. Auger, M. L. Begemann-Blaich *et al.*, Directed and elliptic flow in $^{197}\text{Au} + ^{197}\text{Au}$ at intermediate energies, *Phys. Lett. B* **608**, 223 (2005).
- [59] A. Andronic, J. Łukasik, W. Reisdorf *et al.*, Systematics of stopping and flow in Au+ Au collisions, *Eur. Phys. J. A* **30**, 31 (2006).
- [60] W. Reisdorf, A. Andronic, R. Averbeck *et al.*, Systematics of central heavy ion collisions in the 1A GeV regime, *Nucl. Phys. A* **848**, 366 (2010).
- [61] P. Carruthers and F. Zachariassen, Quantum collision theory with phase-space distributions, *Rev. Mod. Phys.* **55**, 245 (1983).
- [62] C. Y. Wong, Dynamics of nuclear fluid. VIII. Time-dependent Hartree-Fock approximation from a classical point of view, *Phys. Rev. C* **25**, 1460 (1982).
- [63] G. Ruetsch and M. Fatica, *CUDA Fortran for Scientists and Engineers: Best Practices for Efficient CUDA Fortran Programming* (Morgan Kaufmann, Burlington, MA, 2013).
- [64] J. Bartel, P. Quentin, M. Brack *et al.*, Towards a better parametrisation of Skyrme-like effective forces - A critical study of the SkM force, *Nucl. Phys. A* **386**, 79 (1982).
- [65] G. Mao, Z. Li, Y. Zhuo, Y. Han, and Z. Yu, Study of in-medium NN inelastic cross section from relativistic Boltzmann-Uehling-Uhlenbeck approach, *Phys. Rev. C* **49**, 3137 (1994).
- [66] N. Dinh Dang, Shear-viscosity to entropy-density ratio from giant dipole resonances in hot nuclei, *Phys. Rev. C* **84**, 034309 (2011).
- [67] A. Bracco, F. Camera, M. Mattiuzzi *et al.*, Increase in width of the giant dipole resonance in hot nuclei: shape change or collisional damping? *Phys. Rev. Lett.* **74**, 3748 (1995).
- [68] A. Bonasera, V. N. Kondratyev, A. Smerzi, E. A. Remler *et al.*, Nuclear dynamics in the Wigner representation, *Phys. Rev. Lett.* **71**, 505 (1993).
- [69] W. B. He, Y. G. Ma, X. G. Cao, X. Z. Cai, and G. Q. Zhang, Giant dipole resonance as a fingerprint of α clustering configurations in ^{12}C and ^{16}O , *Phys. Rev. Lett.* **113**, 032506 (2014).
- [70] B. S. Huang and Y. G. Ma, Dipole excitation of ^6Li and ^9Be studied with an extended quantum molecular dynamics model, *Phys. Rev. C* **103**, 054318 (2021).
- [71] S. S. Wang, Y. G. Ma, W. B. He, D. Q. Fang, and X. G. Cao, Influences of α -clustering configurations on the giant dipole resonance in hot compound systems, *Phys. Rev. C* **108**, 014609 (2023).
- [72] M. Urban, Pygmy resonance and torus mode within Vlasov dynamics, *Phys. Rev. C* **85**, 034322 (2012).
- [73] H. Zheng, S. Burrello, M. Colonna *et al.*, Dipole response in neutron-rich nuclei with new Skyrme interactions, *Phys. Rev. C* **94**, 014313 (2016).
- [74] A. L. Fetter and J. D. Walecka, *Quantum Theory of Many-Particle Systems* (McGraw-Hill, New York, 1971).
- [75] B. Hong, Nuclear stopping at SIS energies by using isospin asymmetric nuclear collisions, *Nucl. Phys. A* **721**, C317 (2003).
- [76] G. Q. Zhang, Y. G. Ma, X. G. Cao, C. L. Zhou, X. Z. Cai, D. Q. Fang, W. D. Tian, and H. W. Wang, Unified description of nuclear stopping in central heavy-ion collision from 10A MeV to 1.2A GeV, *Phys. Rev. C* **84**, 034612 (2011).
- [77] J. Łukasik, S. Hudan, F. Lavaud *et al.*, Transverse velocity scaling in $^{197}\text{Au} + ^{197}\text{Au}$ fragmentation, *Phys. Rev. C* **66**, 064606 (2002).

- [78] J. Dobaczewski, W. Nazarewicz, and P. G. Reinhard, Error estimates of theoretical models: A guide, *J. Phys. G: Nucl. Part. Phys.* **41**, 074001 (2014).
- [79] Z. R. Hao, G. T. Fan, H. W. Wang *et al.*, Collimator system of SLEGS beamline at Shanghai Light Source, *Nucl. Instrum. Methods Phys. Res. A* **1013**, 165638 (2021).
- [80] H. W. Wang, G. T. Fan, L. X. Liu *et al.*, Commissioning of laser electron gamma beamline SLEGS at SSRF, *Nucl. Sci. Tech.* **33**, 87 (2022).
- [81] K. J. Chen, L. X. Liu, Z. R. Hao *et al.*, Simulation and test of the SLEGS TOF spectrometer at SSRF, *Nucl. Sci. Tech.* **34**, 47 (2023).